Nonmonotonic Constitutive Curves and Shear Banding in Dry and Wet Granular Flows

Christopher Ness[1] and Suzanne M. Fielding[2]
[1]School of Engineering, University of Edinburgh, Edinburgh EH9 3FG, United Kingdom
[2]Department of Physics, Durham University, Science Laboratories, South Road, Durham DH1 3LE, United Kingdom

(Received 4 July 2024; accepted 10 December 2024; published 21 January 2025)

We use particle simulations to map comprehensively the shear rheology of dry and wet granular matter comprising particles of finite stiffness, in both fixed pressure and fixed volume protocols. At fixed pressure we find nonmonotonic constitutive curves that are shear thinning, whereas at fixed volume we find nonmonotonic constitutive curves that are shear thickening. We show that the presence of one nonmonotonicity does not imply the other. Instead, there exists a signature in the volume fraction measured under fixed pressure that, when present, ensures nonmonotonic constitutive curves at fixed volume. In the context of dry granular flow we show that gradient and vorticity bands arise under fixed pressure and volume, respectively, as implied by the constitutive curves. For wet systems our results are consistent with a recent experimental observation of shear thinning at fixed pressure. We furthermore predict discontinuous shear thickening in the absence of critical load friction.

DOI: 10.1103/PhysRevLett.134.038201

Dense granular packings, both dry and suspended in liquid, are among the most abundant materials on Earth. They are relevant to manifold geophysical phenomena, e.g., landslides and debris flows [1,2], and to industrial processes such as paste extrusion [3,4]. Understanding their deformation and flow properties is thus of major practical importance. It is also of fundamental interest in statistical physics, fluid mechanics, and rheology [5–8].

For any complex fluid, a key rheological fingerprint is the constitutive relation of shear stress σ_{xy} as a function of shear rate $\dot{\gamma}$ in stationary homogeneous shear. For granular materials, there exist two paradigmatic protocols for characterizing this relation. In the first ("fixed volume") [9–14], one fixes the sample volume V and measures σ_{xy} (and sometimes the normal stress or normal stress differences) as a function of $\dot{\gamma}$ at a given particle volume fraction ϕ. In the second ("fixed pressure"), one fixes the external pressure (usually in fact the normal particle stress σ_{yy}, but see Ref. [15]) and allows ϕ to vary while measuring σ_{xy} as a function of $\dot{\gamma}$.

In the fixed-V protocol, dry systems display distinct quasistatic, intermediate, and inertial flow regimes dependent on $\dot{\gamma}$ and ϕ [11]. In suspensions the inertial regime is replaced by a viscous regime [16,17]. Hysteresis is often observed close to the jamming volume fraction ϕ_{m} that marks the transition between quasistatic and inertial or viscous regimes, suggesting that the constitutive curve $\sigma_{xy}(\dot{\gamma})$ has a shear-thickening, S-shaped nonmonotonicity. In the unstable region σ_{xy} can adopt multiple values at a single $\dot{\gamma}$ [18–20], implying a predisposition to vorticity banding [21].

In the fixed-σ_{yy} protocol, experimental data for the macroscopic friction $\mu = \sigma_{xy}/\sigma_{yy}$ across a range of scaled shear rates ("inertial number") $I = \dot{\gamma}a/\sqrt{\sigma_{yy}/\rho}$ [22] suggests universal constitutive relations $\mu(I)$ and $\phi(I)$ in dry systems [23,24]. Here a and ρ are the particle radius and density. Recent innovations enabling fixed-σ_{yy} measurements in suspensions [25,26] remarkably suggest analogous relations $\mu(J)$ and $\phi(J)$, with $J = \eta\dot{\gamma}/\sigma_{yy}$ now the "viscous number," where η is the solvent viscosity [25,27]. In slow shear (small I, J), μ was shown to decrease with increasing I in dry simulations [28] and experiments [29] (see also [30–33]), and likewise suggested to decrease with increasing J in experiments on wet systems [34], before increasing at large I, J. This gives a shear-thinning nonmonotonicity, in which $\dot{\gamma}$ can adopt multiple values at a single μ, implying a predisposition to gradient banding.

In this Letter, we advance the understanding of granular rheology in three key directions. First, we demonstrate, within a single model granular system, constitutive curves that are nonmonotonic and shear thinning (thickening) at fixed σ_{yy} (fixed V), and show a mapping whereby data can be transposed between these two representations. Significantly, we find that nonmonotonicity at fixed σ_{yy} does not imply the same at fixed V, uncovering instead a signature in the fixed-σ_{yy} curves $\phi(I)$ [or $\phi(J)$] that, if present, implies nonmonotonic $\sigma_{xy}(\dot{\gamma})$ at fixed V. Second, we show in the context of dry granular systems shear bands with layer normals in the gradient direction at fixed σ_{yy}, and

vorticity direction at fixed V, revealing a predisposition toward heterogeneous flow consistent with the measured constitutive curves. Third, we provide the first simulation evidence for nonmonotonic $\mu(J)$ in suspensions, recently suggested experimentally [34], and show that discontinuous shear thickening (DST) can arise at fixed V even in the absence of critical load friction [35,36], hitherto considered prerequisite.

Simulation—We simulate the Newtonian dynamics of a packing of spheres of density ρ with bidisperse radii a and $1.4a$ (chosen to prevent crystallization [37]) using LAMMPS [38–40]. Interparticle contacts are modeled as Hookean with stiffness k, frictional with sliding coefficient $\mu_p = 0.5$, and damped with normal and tangential restitution coefficient 0.5. We verified that varying k over an order of magnitude does not significantly change any of our results. For wet systems we also implement pairwise lubrication forces. Between any two particles α and β the leading term for particle α is $F_i^\alpha = (\kappa/h)n_i n_j(u_j^\beta - u_j^\alpha)$ with κ a scalar function of the radii [41], n the center-to-center unit vector, u^α and u^β the particle velocities, and h the surface-to-surface distance. (Roman suffices denote Cartesian directions.) The force is truncated when $h < 10^{-3}a$. For details, see Ref. [40].

We impose simple shear of rate $\dot\gamma = \partial v_x/\partial y$ via Lees-Edwards boundaries [42], with flow, gradient, and vorticity directions x, y, and z. Our time unit $\tau_I = \sqrt{\rho a^3/k}$ and $\tau_V = \eta a/k$ in dry and wet systems, respectively, giving nondimensional shear rates $\dot\gamma_d = \dot\gamma\tau_I$ and $\dot\gamma_w = \dot\gamma\tau_V$. The stress is computed by averaging the tensor product of particle-particle vectors and forces, and rescaled as $\Sigma_{ij} = \sigma_{ij}a/k$, so that $\mu = \Sigma_{xy}/\Sigma_{yy}$, $I = \dot\gamma_d/\sqrt{\Sigma_{yy}}$, and $J = \dot\gamma_w/\Sigma_{yy}$. Steady state data are averaged over 30 realizations measured up to 10 strain units beyond the initial transient. Results are independent of our time step, $\delta t = 0.01\tau_I$. The periodic box size $L_{x,y,z} \approx 30a$ in Figs. 1 and 4, with elongated L_y or L_z specified in Figs. 2 and 3.

To model the experimental protocols described above, we perform simulations in two different modes. In one we fix V (and so ϕ) and $\dot\gamma$, measuring Σ_{xy} and Σ_{yy} in steady state. In the other we fix $\dot\gamma$ and introduce a set point normal stress Σ_{yy}^{SP}, at each time step updating $V(t+\delta t) = V(t) + \alpha\delta t(\Sigma_{yy}(t) - \Sigma_{yy}^{SP})/\Sigma_{yy}^{SP}$ and checking that this maintains $\Sigma_{yy} \approx \Sigma_{yy}^{SP}$ to excellent approximation. We set $\alpha = 0.1$ having verified that results are insensitive to this choice. We then measure ϕ and Σ_{xy} in steady state.

Dry system—We start with the fixed-Σ_{yy} data. Figures 1(a)–1(d) show constitutive curves $\mu(I)$ and $\phi(I)$ obtained for several fixed Σ_{yy} by increasing $\dot\gamma_d$ (and so $I = \dot\gamma_d/\sqrt{\Sigma_{yy}}$) from left to right. Figure 1(e) shows that our control scheme produces a stable Σ_{yy} over time. Viewed on the coarse scale of Figs. 1(a) and 1(c), the rheology is broadly consistent with that for hard particles, with master curves for $\mu(I)$ and $\phi(I)$ following [22,25]. However, the separation of μ and ϕ curves on the finer scales of Figs. 1(b) and 1(d), and the anomalous ϕ curves in Fig. 1(c) (red lines), shows a breakdown of this master scaling for larger Σ_{yy}. The finite stiffness k in our model allows particles to be slightly compressed, meaning the flow state is not uniquely defined by I but depends separately on $\dot\gamma_d$ and Σ_{yy}. The $\mu(I)$ curves obtained by increasing $\dot\gamma_d$ at fixed Σ_{yy} are then nonmonotonic, with a window of I over which $(\partial\mu/\partial I)|_{\Sigma_{yy}} < 0$ (pink boxes, Fig. 1), consistent with an earlier result in 2D [28]. This suggests that flow at an imposed global I in this window will form gradient shear bands of differing $\dot\gamma_d$ with layer normals along y. Meanwhile, the $\phi(I)$ data in Fig. 1(d) reveal dilation with increasing $\dot\gamma_d$ at fixed Σ_{yy}, with $(\partial\phi/\partial I)|_{\Sigma_{yy}} < 0$.

In this regime, where the flow depends not on I alone but on both $\dot\gamma_d$ and Σ_{yy}, one can obtain constitutive curves at fixed Σ_{yy} by varying $\dot\gamma_d$ (as discussed so far) or at fixed $\dot\gamma_d$ by varying Σ_{yy}. To explore the latter, we show by the purple line in Fig. 1(d) all data points with a single fixed $\dot\gamma_d$, now across data for different Σ_{yy}. Doing so reveals another nonmonotonicity, highlighted by the green boxes in Fig. 1, with a window of I for which $(\partial\phi/\partial I)|_{\dot\gamma_d} > 0$, which means that increasing Σ_{yy} causes dilation. This will have important implications for the fixed-V rheology, to which we now turn.

Shown in Fig. 1(f) are time-dependent signals $\Sigma_{xy}(t)$ measured at a given $\dot\gamma_d$ for three ϕ. Beyond the $\dot\gamma t \le 1$ start-up transient, we observe a statistically steady Σ_{xy} for $\phi = 0.58,\ 0.61$. In contrast, at intermediate $\phi = 0.596$ the stress intermittently switches between two apparently metastable values, each sustained for 0.5–2 strain units. Similar phenomenology was seen in [11], described there as fluctuating rather than bistable behavior. Running our simulation at $\phi = 0.596$ and imposed Σ_{xy} (using an algorithm analogous to our fixed-Σ_{yy} one) led to flow arrest at long times as reported previously [18,43], precluding fixed-V measurement of the unstable region. To obtain a point (or points) on the stationary constitutive curve from this $\Sigma_{xy}(t)$ signal at each $\dot\gamma_d$ and ϕ, we produce a histogram $P(\Sigma_{xy})$ by sampling at intervals of $\dot\gamma t = 0.01$, and fit it to a single Gaussian for low and high ϕ, or a sum of two Gaussians for bistable cases at intermediate ϕ. The locations of the maximum (or maxima) of these fits are taken as the time-averaged stress values, shown by solid colored lines in Figs. 1(g) and 1(h).

We additionally obtain *reconstructed* fixed-V constitutive curves from the fixed-Σ_{yy} data presented in Figs. 1(a)–1(d). Each plotted point therein has known μ, ϕ, and I, with the latter measured at known Σ_{yy} and $\dot\gamma_d$ and with $\Sigma_{xy} = \mu\Sigma_{yy}$. We thus replot these data $\Sigma_{xy}(\dot\gamma_d)$ and $\Sigma_{yy}(\dot\gamma_d)$ as faded colored lines in Figs. 1(g) and 1(h). Here $\Sigma_{yy}(\dot\gamma_d)$ are horizontal lines along which ϕ decreases monotonically from left to right. Connecting points on each of these lines that have equal ϕ, one obtains the solid gray and black

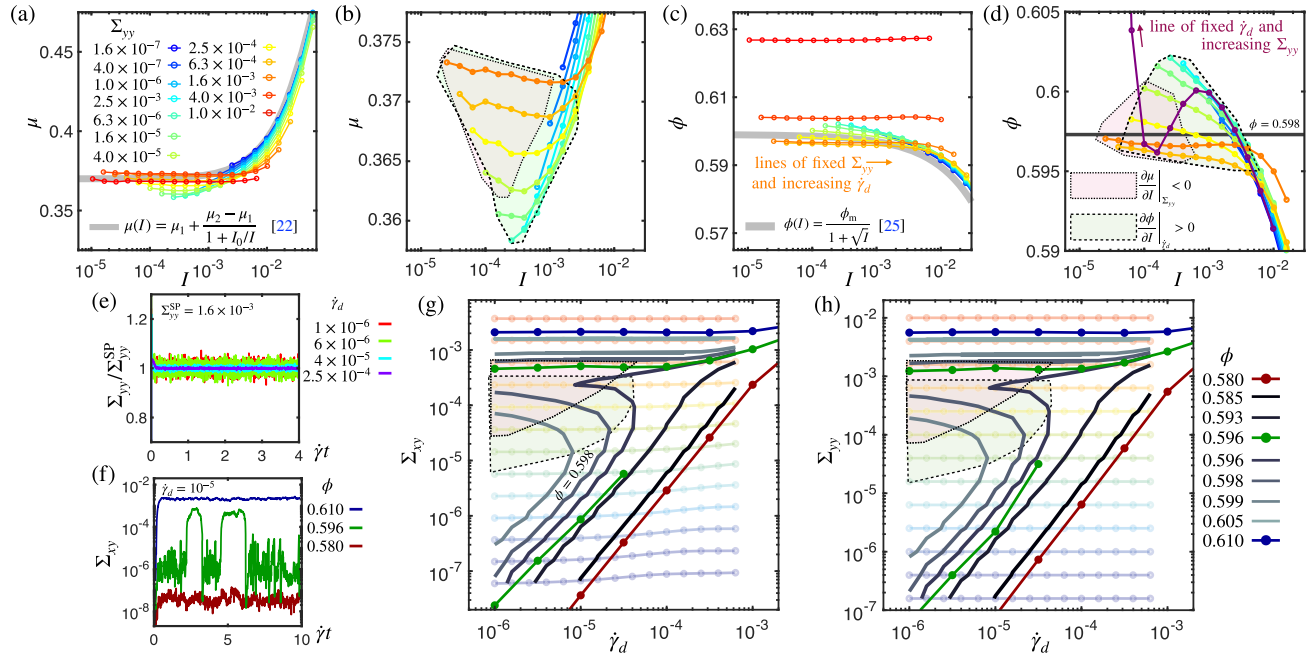

FIG. 1. Nonmonotonic constitutive curves of dry granular material at fixed Σ_{yy} (a)–(e) and fixed V (f)–(h). Shown are (a) $\mu(I)$ and (c) $\phi(I)$, respectively, enlarged in (b) and (d). Each curve of color blue to red has increasing $\dot{\gamma}_d$ left to right at a fixed Σ_{yy} shown by the legend in (a). Purple line in (d) connects points with $\dot{\gamma}_d = 4 \times 10^{-6}$ and varying Σ_{yy}. Broad gray lines show fits of [22] (a) and [25] (c). Our fixed-Σ_{yy} feedback algorithm maintains a setpoint $\Sigma_{yy}^{SP} = 1.6 \times 10^{-3}$ over time (e). In (f) are fixed-V time series of Σ_{xy} at $\dot{\gamma}_d = 10^{-5}$ for various ϕ. In (g) and (h) we first replot fixed-Σ_{yy} data from (a)–(d) as faded lines blue to red, then connect points of equal ϕ on these curves by lines gray to black. This gives fixed-V constitutive curves, reconstructed from the fixed-Σ_{yy} data. Shown by darker red, green, and blue lines in (g) and (h) are constitutive curves measured actually at fixed V, by binning time series of Σ_{xy} [shown in (f)] and Σ_{yy} as described in the text. Shaded boxes in (b), (d), (g), and (h) cover regimes that have $(\partial\mu/\partial I)|_{\Sigma_{yy}} < 0$ (pink) and $(\partial\phi/\partial I)|_{\dot{\gamma}_d} > 0$ (green), transcribed across fixed-Σ_{yy} and fixed-V protocols.

contours in Figs. 1(g) and 1(h). For low $\dot{\gamma}_d$ we observe inertial $\Sigma_{xy} = f(\phi)\dot{\gamma}_d{}^2$ rheology [11,44] for $\phi \leq 0.593$ and quasistatic $\Sigma_{xy} = h(\phi)$ for $\phi \geq 0.605$. For large $\dot{\gamma}_d$ the data tend toward intermediate $\Sigma_{xy} \sim \dot{\gamma}_d{}^{1/2}$ behavior [11]. This reconstruction produces constitutive curves that are S shaped and show DST, consistent with the bivalued constitutive curves obtained for $0.596 \leq \phi \leq 0.599$ in the fixed-V simulation. The particle contact number grows toward its isostatic point $z \approx 4$ (for our μ_p) with increasing stress at fixed V (data not shown). Importantly, this suggests a different DST mechanism compared to critical load models in which the isostatic point itself decreases with increasing stress [35,36]. Indeed, the transition reported here links inertial or viscous branches to quasistatic ones, as opposed to linking frictionless and frictional viscous branches as in [35,36].

We now show that these S-shaped $\Sigma_{yy}(\dot{\gamma}_d)$ curves map directly to a particular feature of $\phi(I)$ in Fig. 1(d). Writing $\phi = f(\dot{\gamma}_d, \Sigma_{yy})$, one can find the slope of fixed-V curves by setting $d\phi = 0$ and using the definition of I to obtain $(d\Sigma_{yy}/d\dot{\gamma}_d)|_\phi = (2\Sigma_{yy}/\dot{\gamma}_d)[(\partial f/\partial I)|_{\Sigma_{yy}}]/[(\partial f/\partial I)|_{\dot{\gamma}_d}]$ [45]. Thus if $(\partial\phi/\partial I)|_{\Sigma_{yy}} < 0$ [blue-to-red lines, Fig. 1(d)], then $(\partial\phi/\partial I)|_{\dot{\gamma}_d} > 0$ (purple line) implies downward sloping fixed-V curves $\Sigma_{yy}(\dot{\gamma}_d)$. Indeed, the green boxes in Fig. 1 defined by $(\partial\phi/\partial I)|_{\dot{\gamma}} > 0$ coincide in Figs. 1(g) and 1(h) with $(\partial\Sigma_{yy}/\partial\dot{\gamma})|_\phi < 0$ (and $(\partial\Sigma_{xy}/\partial\dot{\gamma})|_\phi < 0$). The same conclusion may be obtained graphically, by taking a horizontal line through Fig. 1(d) at, say, $\phi = 0.598$ (dark gray line). One now finds three intersections with the purple line, giving three stress states for a given $\dot{\gamma}_d$ at $\phi = 0.598$, implying S-shaped fixed-V constitutive curves. Importantly, the pink and green boxes do not fully overlap, so that nonmonotonic $\mu(I)$ (pink) and $\Sigma_{xy}(\dot{\gamma})$ (green) do not imply each other.

So far, we have reported constitutive curves that are nonmonotonic and shear thinning at fixed Σ_{yy}, implying a predisposition toward gradient banding, and, in notable contrast, nonmonotonic and shear thickening at fixed ϕ, implying a predisposition toward vorticity banding. Significantly, fixed-Σ_{yy} simulations with $\mu_p = 0$ produce monotonic $\mu(I)$ and $\phi(I)$. We now show that the observed nonmonotonicities indeed lead to the formation of bands in simulation boxes large enough to accommodate heterogeneity along the relevant axis. (The boxes simulated in Fig. 1 are too small to do so.)

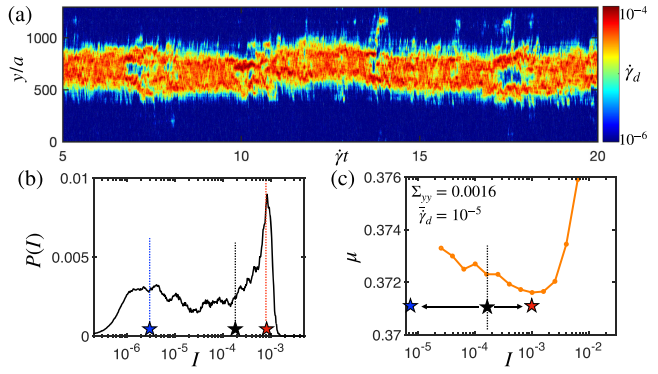

FIG. 2. Gradient banding in dry system. (a) Strain series of $\dot{\gamma}_d$ profile across y, measured at fixed global $\Sigma_{yy} = 0.0016$ and $\bar{\dot{\gamma}}_d = 10^{-5}$. Binning temporal and spatial I data gives the histogram in (b). From its peaks we obtain I in the low (blue star) and high (red star) shear regions. These are then plotted as $\mu(I)$ in (c). Orange line in (c) represents the homogeneous $\mu(I)$ at $\Sigma_{yy} = 0.0016$ from Fig. 1(a). Dashed black lines in (b) and (c) indicate imposed global I.

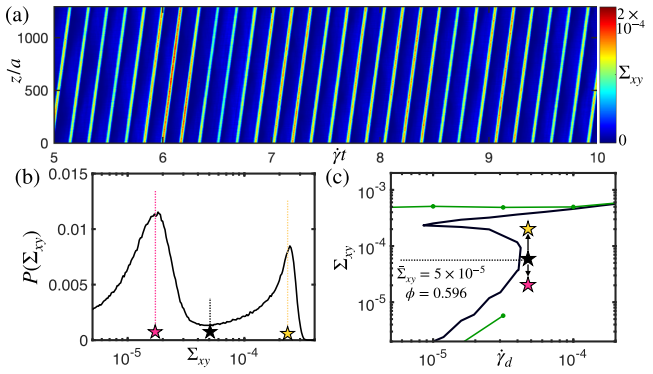

FIG. 3. Vorticity banding in dry system. (a) Strain series of Σ_{xy} profile across z measured at fixed global $\phi = 0.596$ and $\bar{\Sigma}_{xy} = 5 \times 10^{-5}$. Binning temporal and spatial Σ_{xy} leads to the histogram in (b). From its peaks we obtain the low (pink star) and high (yellow star) Σ_{xy} values, plotted in (c) with those obtained under fixed V and under the reconstruction [green and black lines, Fig. 1(g)] at the same ϕ. Dashed black lines in (b) and (c) indicate imposed global $\bar{\Sigma}_{xy}$.

Figure 2 shows a simulation at fixed Σ_{yy} in a box elongated along the gradient direction, $L_y = 1200a$. The stress Σ_{yy} is such that the $\mu(I)$ curve for homogeneous shear (in a smaller box) is nonmonotonic, Fig. 2(c). A global shear rate $\bar{\dot{\gamma}}_d$ is then imposed so that I lies in its negatively sloping part (black star). The time series of the y profile of $\dot{\gamma}_d$ then clearly reveals banding, Fig. 2(a). Binning the local I values gives the histogram in Fig. 2(b), with peaks at I values indicated by the blue and red stars in Figs. 2(b) and 2(c). These show that the low shear band is effectively jammed ($I \approx 0$) while the high shear band lies close to the minimum of the homogeneous $\mu(I)$. The stress values remain spatially and temporally uniform (not shown), with μ in the banded state slightly below that in homogeneous flow, Fig. 2(c). This may be due to nonlocal effects, which are known to cause deviations from homogeneous rheology that propagate distances $\mathcal{O}(10)a$ from yield planes [46].

Figure 3 reports a fixed-V simulation in a box elongated along the vorticity direction, $L_z = 1200a$, with $\phi = 0.596$ so that $\Sigma_{xy}(\dot{\gamma}_d)$ is nonmonotonic, Fig. 3(c). A setpoint global stress $\bar{\Sigma}_{xy}$ (black star) is imposed near its negatively sloping part via an algorithm that dynamically adjusts $\dot{\gamma}_d$. The time series of the z profile of Σ_{xy}, Fig. 3(a) (and Σ_{yy}, not shown), then also shows a stress band. This is not, however, stationary but steadily propagates along z, consistent with the balance of normal stresses precluding stationary banding [47]. The ϕ profile is uniform throughout, within the sensitivity of our measurement. Binning the Σ_{xy} data gives the histogram in Fig. 3(b), with peaks at Σ_{xy} values (pink and yellow stars) transcribed to the $\Sigma_{xy}(\dot{\gamma}_d)$ representation in Fig. 3(c). This finding is contrary to a report in 2D dry systems of a homogeneous jammed state in regions where $\Sigma_{xy}(\dot{\gamma}_d)$ is expected to be downward sloping [18]. Propagating vorticity bands were, however, seen (albeit for wet systems with critical load friction) in [48].

Wet system—We show finally that constitutive curves for wet systems have nonmonotonicities counterpart to those in dry systems. Figure 4(a) shows that $\mu(J)$ curves obtained by varying $\dot{\gamma}_w$ at fixed Σ_{yy} are nonmonotonic for a range (albeit limited) of Σ_{yy}. The $\phi(J)$ curve measured by instead varying Σ_{yy} at fixed $\dot{\gamma}_w$ is also nonmonotonic [purple line, Fig. 4(b)]. This then maps to nonmonotonic reconstructed S-shaped shear-thickening curves $\Sigma_{xy}(\dot{\gamma}_w)$ and $\Sigma_{yy}(\dot{\gamma}_w)$ at

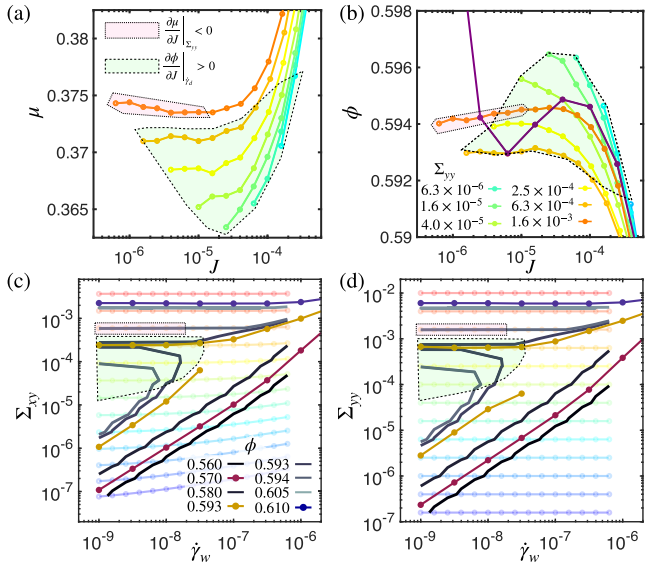

FIG. 4. Nonmonotonic constitutive curves of wet granular material. Shown in (a) and (b) are $\mu(J)$ and $\phi(J)$; in (c) and (d) are the same data along with reconstructed and actual fixed-V data obtained equivalently to those in Fig. 1.

fixed V in Figs. 4(c) and 4(d), as for dry systems. Simulations performed actually at fixed V in this regime likewise give bivalued constitutive curves [49], with a viscous regime $\Sigma_{xy} \propto \dot{\gamma}_w$ for $\phi \leq 0.58$.

For dry systems, we recall that negative slope of the μ curves at fixed Σ_{yy} (pink boxes, Fig. 1) does not automatically imply negative slope of the $\Sigma_{xy}(\dot{\gamma}_w)$ curves at fixed V (green boxes). This lack of correspondence is even more apparent in wet systems: little overlap is apparent between the pink and green boxes in Fig. 4. Instead, as in dry systems, the presence of negative slope in the constitutive curves $\Sigma_{xy}(\dot{\gamma}_w)$ at fixed V requires only that the material is dilatant with respect to increases in both $\dot{\gamma}_w$ and Σ_{yy} under fixed Σ_{yy}. Grob *et al.* [18] give a criterion for the existence of such points based on a simple model of additive stress contributions to $\dot{\gamma}$.

Conclusion—In this Letter, we have mapped the fixed-Σ_{yy} and fixed-V constitutive curves of wet and dry granular flows, shown the mapping between them, and demonstrated their connection to shear banding. Our results highlight the shortcomings of current constitutive models: predictions for S-shaped $\Sigma_{xy}(\dot{\gamma})$ exist, but do not predict nonmonotonicity in μ [18,36,50] or incorporate quasistatic flow. A phenomenological model encoding flow-induced noise predicts nonmonotonic $\mu(I)$ [28], though the demonstration of nonmonotonic $\mu(J)$ calls for an equivalent mechanism to be identified in overdamped systems. Further, our results challenge the present consensus by showing that DST can arise in the absence of a critical load model [35,36], with finite stiffness alone providing the requisite stress scale. This informs an ongoing debate on whether contacts of few asperities render deformations relevant even for grains of large modulus [51–54]. Reconciling the rich banding dynamics reported here with a detailed mechanistic description accounting also for nonlocality [32,46] and boundary effects [55] is an open challenge. Relating underlying constitutive curves to measured flow curves is a long-standing problem in complex fluids, reinvigorated by our demonstration here that the measurement protocol can radically change the observed phenomenology. Further understanding the micromechanics at play is a fundamental challenge to statistical and soft matter physics, and to developing rheological constitutive models crucial to predicting macroscopic engineering flows.

Acknowledgments—The authors thank M. Cates and Y. Jiang for discussions. This project has received funding from the European Research Council (ERC) under the European Union's Horizon 2020 research and innovation programme (Grant Agreement No. 885146) (S. M. F.), and from the Royal Academy of Engineering under the Research Fellowship scheme and from the Leverhulme Trust under Research Project Grant No. RPG-2022-095 (C. N.).

[1] R. M. Iverson, Rev. Geophys. **35**, 245 (1997).
[2] K. Hutter, Phil. Trans. R. Soc. A **363**, 1497 (2005).
[3] R. O'Neill, H. McCarthy, E. Montufar, M.-P. Ginebra, D. Wilson, A. Lennon, and N. Dunne, Acta Biomater. **50**, 1 (2017).
[4] K. Prabha, P. Ghosh, S. Abdullah, R. M. Joseph, R. Krishnan, S. S. Rana, and R. C. Pradhan, Future Foods **3**, 100019 (2021).
[5] É. Guazzelli and O. Pouliquen, J. Fluid Mech. **852**, P1 (2018).
[6] Y. Forterre and O. Pouliquen, Annu. Rev. Fluid Mech. **40**, 1 (2008).
[7] H. M. Jaeger, S. R. Nagel, and R. P. Behringer, Rev. Mod. Phys. **68**, 1259 (1996).
[8] C. Ness, R. Seto, and R. Mari, Annu. Rev. Condens. Matter Phys. **13**, 97 (2022).
[9] P. Olsson and S. Teitel, Phys. Rev. Lett. **99**, 178001 (2007).
[10] M. Otsuki and H. Hayakawa, Phys. Rev. E **80**, 011308 (2009).
[11] S. Chialvo, J. Sun, and S. Sundaresan, Phys. Rev. E **85**, 021305 (2012).
[12] H. de Cagny, A. Fall, M. M. Denn, and D. Bonn, J. Rheol. **59**, 957 (2015).
[13] K. N. Nordstrom, E. Verneuil, P. E. Arratia, A. Basu, Z. Zhang, A. G. Yodh, J. P. Gollub, and D. J. Durian, Phys. Rev. Lett. **105**, 175701 (2010).
[14] B. M. Guy, M. Hermes, and W. C. K. Poon, Phys. Rev. Lett. **115**, 088304 (2015).
[15] I. Srivastava, L. E. Silbert, G. S. Grest, and J. B. Lechman, J. Fluid Mech. **907**, A18 (2021).
[16] M. Trulsson, B. Andreotti, and P. Claudin, Phys. Rev. Lett. **109**, 118305 (2012).
[17] C. Ness and J. Sun, Phys. Rev. E **91**, 012201 (2015).
[18] M. Grob, C. Heussinger, and A. Zippelius, Phys. Rev. E **89**, 050201(R) (2014).
[19] S. Saw, M. Grob, A. Zippelius, and C. Heussinger, Phys. Rev. E **101**, 012602 (2020).
[20] M. Otsuki and H. Hayakawa, Phys. Rev. E **83**, 051301 (2011).
[21] P. D. Olmsted, Rheol. Acta **47**, 283 (2008).
[22] P. Jop, Y. Forterre, and O. Pouliquen, Nature (London) **441**, 727 (2006).
[23] G. D. R. MiDi, Eur. Phys. J. E **14**, 341 (2004).
[24] A. Fall, G. Ovarlez, D. Hautemayou, C. Mézière, J.-N. Roux, and F. Chevoir, J. Rheol. **59**, 1065 (2015).
[25] F. Boyer, É. Guazzelli, and O. Pouliquen, Phys. Rev. Lett. **107**, 188301 (2011).
[26] B. Etcheverry, Y. Forterre, and B. Metzger, Phys. Rev. X **13**, 011024 (2023).
[27] F. Tapia, O. Pouliquen, and É. Guazzelli, Phys. Rev. Fluids **4**, 104302 (2019).
[28] E. DeGiuli and M. Wyart, Proc. Natl. Acad. Sci. U.S.A. **114**, 9284 (2017).
[29] J. A. Dijksman, G. H. Wortel, L. T. H. van Dellen, O. Dauchot, and M. Van Hecke, Phys. Rev. Lett. **107**, 108303 (2011).
[30] H. Jaeger, C.-H. Liu, S. Nagel, and T. Witten, Europhys. Lett. **11**, 619 (1990).
[31] P. Mills, P. Rognon, and F. Chevoir, Europhys. Lett. **81**, 64005 (2008).

[32] S. Mowlavi and K. Kamrin, Soft Matter **17**, 7359 (2021).
[33] F. Da Cruz, F. Chevoir, D. Bonn, and P. Coussot, Phys. Rev. E **66**, 051305 (2002).
[34] H. Perrin, C. Clavaud, M. Wyart, B. Metzger, and Y. Forterre, Phys. Rev. X **9**, 031027 (2019).
[35] R. Seto, R. Mari, J. F. Morris, and M. M. Denn, Phys. Rev. Lett. **111**, 218301 (2013).
[36] M. Wyart and M. E. Cates, Phys. Rev. Lett. **112**, 098302 (2014).
[37] C. S. O'Hern, L. E. Silbert, A. J. Liu, and S. R. Nagel, Phys. Rev. E **68**, 011306 (2003).
[38] C. Ness, Comput. Part. Mech. **10**, 2031 (2023).
[39] A. P. Thompson, H. M. Aktulga, R. Berger, D. S. Bolintineanu, W. M. Brown, P. S. Crozier, P. J. in't Veld, A. Kohlmeyer, S. G. Moore, T. D. Nguyen *et al.*, Comput. Phys. Commun. **271**, 108171 (2022).
[40] O. Cheal and C. Ness, J. Rheol. **62**, 501 (2018).
[41] D. Jeffrey, Phys. Fluids A **4**, 16 (1992).
[42] A. W. Lees and S. F. Edwards, J. Phys. C **5**, 1921 (1972).
[43] M. Grob, A. Zippelius, and C. Heussinger, Phys. Rev. E **93**, 030901(R) (2016).
[44] C. S. Campbell, Annu. Rev. Fluid Mech. **22**, 57 (1990).
[45] Using $I = \dot{\gamma}/\sqrt{\Sigma_{yy}}$ we obtain $\partial\dot{\gamma}|_{\Sigma_{yy}} = \sqrt{\Sigma_{yy}}\partial I|_{\Sigma_{yy}}$ and $\partial\Sigma_{yy}|_{\dot{\gamma}} = [(-2\Sigma_{yy}^{3/2})/\dot{\gamma}]\partial I|_{\dot{\gamma}}$, which when substituted into the total derivative $d\phi = (\partial f/\partial\dot{\gamma})|_{\Sigma_{yy}} d\dot{\gamma} + (\partial f/\partial\Sigma_{yy})|_{\dot{\gamma}} d\Sigma_{yy} = 0$ yields the expression given in the main text.
[46] M. Bouzid, M. Trulsson, P. Claudin, E. Clément, and B. Andreotti, Phys. Rev. Lett. **111**, 238301 (2013).
[47] M. Hermes, B. M. Guy, W. C. K. Poon, G. Poy, M. E. Cates, and M. Wyart, J. Rheol. **60**, 905 (2016).
[48] R. N. Chacko, R. Mari, M. E. Cates, and S. M. Fielding, Phys. Rev. Lett. **121**, 108003 (2018).
[49] The range of ϕ for which inaccessible stress states are observed differs between the dry and wet cases, suggesting that the lubrication forces present in the latter system slightly change ϕ_m.
[50] H. Nakanishi, S. I. Nagahiro, and N. Mitarai, Phys. Rev. E **85**, 011401 (2012).
[51] D. Tabor, J. Lubr. Technol. **103**, 169 (1981).
[52] L. Lobry, E. Lemaire, F. Blanc, S. Gallier, and F. Peters, J. Fluid Mech. **860**, 682 (2019).
[53] R. V. More and A. M. Ardekani, Phys. Rev. E **103**, 062610 (2021).
[54] A. Papadopoulou, J. J. J. Gillissen, H. J. Wilson, M. K. Tiwari, and S. Balabani, J. Non-Newtonian Fluid Mech. **281**, 104298 (2020).
[55] H. Hu, Y. Zhao, W. Zhao, L. Qiao, and Q. Xu, J. Rheol. **68**, 949 (2024).